

1 Ca-isotopes as a robust tracer of magmatic differentiation

2 Hairuo Fu^{1*}, Stein B. Jacobsen¹, Bjørn T. Larsen², Zachary T. Eriksen¹

3 ¹Department of Earth and Planetary Sciences, Harvard University, MA 02138, USA.
4 (*Correspondence to: hairuo.fu@g.harvard.edu)

5 ²Department of Geosciences and CEED, University of Oslo, P.O. Box 1047 Blindern, N-0316
6 Oslo, Norway.

7 Key words: Ca isotopes; Isotope fractionation; Magmatic evolution; Planetary differentiation

8 **Abstract:**

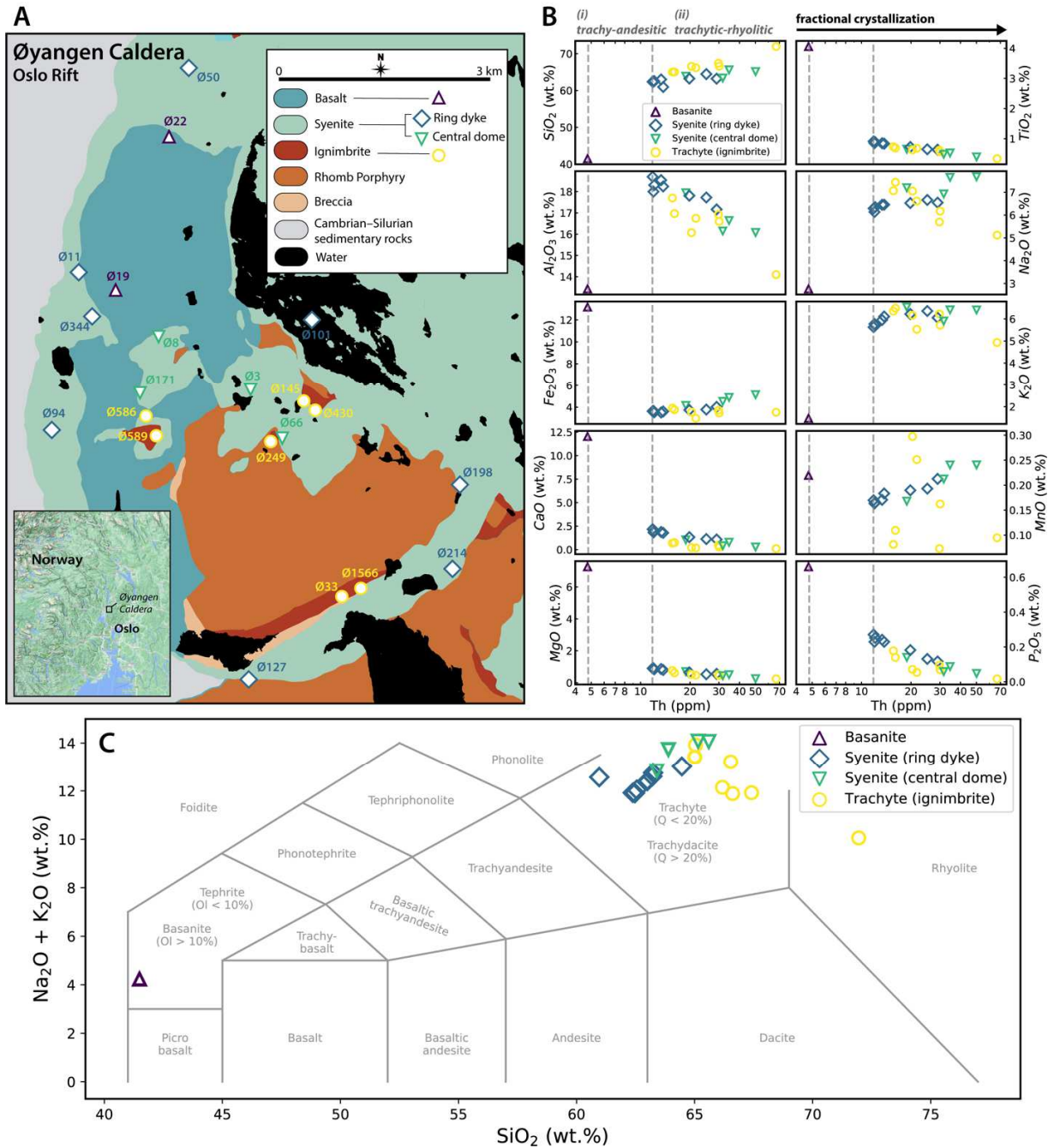
9 The large mass difference (~10%) between the two most abundant isotopes of calcium, ⁴⁰Ca and
10 ⁴⁴Ca, gives Ca great potential in tracking mass-dependent fractionation during magmatic
11 processes. Resolvable Ca-isotope fractionation during fractional crystallization of magma,
12 particularly by feldspar in evolved melts, has been theoretically inferred but not robustly tested
13 in nature. To further explore the effects of magmatic differentiation on Ca-isotope systematics,
14 we studied the late-Permian alkaline igneous suite of the Øyangen Caldera, Oslo Rift, Norway,
15 consisting of volcanic and intrusive units ranging from basaltic to rhyolitic compositions. Major
16 and trace element variations and modeling demonstrate that the main series of samples ($N = 21$),
17 including basanites, ring-dyke syenites, and central-dome syenites, likely documents a co-genetic
18 and closed-system fractional crystallization sequence. Our data show minimal $\delta^{44/40}\text{Ca}$ variation
19 ($< 0.05\text{‰}$) in the intermediate magma and a marked increase in $\delta^{44/40}\text{Ca}$ in the felsic magma of
20 the Øyangen Caldera (from $0.62 \pm 0.02\text{‰}$ to $1.15 \pm 0.03\text{‰}$ relative to Ca standard, SRM915a).
21 The systematic increase is best explained by equilibrium isotopic fractionation dominated by
22 alkali feldspar in the fractionating mineral assemblage. This is further supported by strong
23 correlations between $\delta^{44/40}\text{Ca}$, CaO, and Eu/Eu* in the main-series samples. Implementing a
24 Monte Carlo approach, isotopic modeling of the liquid line of descent using Rayleigh
25 fractionation is highly consistent with the observed Ca-isotope evolution. For the first time, we
26 confirm prominent Ca stable isotope fractionation in felsic-stage differentiation of alkaline
27 magma and constrain the isotope fractionation factors of plagioclase and K-feldspar. Integrated
28 with extant estimations on mineral fractionation factors from the literature, our results suggest
29 increasing fractionation effects of rock-forming minerals with decreasing Ca content. The
30 affirmation of significant Ca-isotope fractionation in alkaline magma by feldspar empowers the
31 application of Ca as a versatile tracer of crustal evolution, allowing further tests in other
32 magmatic conditions across various planetary objects.

33 **1. Introduction**

34 Mass-dependent fractionation of stable isotopes opens a new window in our understanding of
35 magmatic evolution. Although previously perceived as negligible in high-temperature igneous
36 processes (Johnson et al., 2004; Teng et al., 2017), recent advances in high-precision isotope
37 measurements have resolved significant mass fractionation of non-traditional stable isotopes (e.g.,
38 K, Mg, Si, Ca, and Fe) between igneous rocks of different petrogenesis. Such discoveries were
39 attributed to a variety of magmatic processes, such as partial melting, mantle heterogeneity, and
40 igneous differentiation (Huang et al., 2010; Huang et al., 2011, Kang et al., 2017; Schiller et al.,
41 2017; Zhang et al., 2018; Brewer et al., 2018; Wang (王阳) et al., 2019; Valdes et al., 2019;
42 Amsellem et al., 2020; Sun et al. 2021; Zhu et al., 2021; Eriksen and Jacobsen, 2022). Calcium is
43 the fifth most abundant element in Earth's crust and has six stable isotopes (^{40}Ca , ^{42}Ca , ^{43}Ca ,
44 ^{44}Ca , ^{46}Ca , and ^{48}Ca) that exhibit the third-largest relative mass variation (20%) after H and He.
45 The ~10% mass difference between the two most abundant isotopes, ^{40}Ca and ^{44}Ca , makes Ca a
46 valuable candidate for tracking mass fractionation during magmatic differentiation.

47 Calcium-isotope variation during partial melting of mantle rocks (olivine, pyroxene, and garnet
48 dominant) has been extensively studied (e.g., Huang et al., 2010; Kang et al., 2017; Chen et al.,
49 2019), however, Ca-isotope fractionation in crustal magmatic processes (feldspar dominant),
50 especially during fractional crystallization, has remained obscure and controversial. Zhang et al.
51 (2018) analyzed a consecutive sequence of basalts from the Kilauea Iki lava lake, Hawaii,
52 showing no measurable variations of $^{44}\text{Ca}/^{40}\text{Ca}$ (<0.07‰) during crystallization. These results,
53 however, only apply to the mafic to intermediate range of compositions. In contrast, a study of
54 an Archaean ultramafic-mafic-anorthosite igneous complex from the West Africa Craton
55 reported extreme $^{44}\text{Ca}/^{40}\text{Ca}$ isotopic fractionation (~3.2‰) interpreted to be the result of
56 fractional crystallization (Valdes et al., 2019). Nevertheless, the Ca-isotope variation observed
57 from the samples in Valdes et al. (2019) may instead reflect inter-mineral diffusion during
58 metamorphism of the protoliths (peak P-T conditions of 900 °C and 5 kbar) (Valdes et al., 2019;
59 Antonelli and Simon, 2020). More recently, Zhu et al. (2021) found a ~0.2‰ change in
60 $^{44}\text{Ca}/^{40}\text{Ca}$ among the andesitic–rhyolitic volcanic glasses from the eastern Manus Basin,
61 southwestern Pacific. However, their implications hinge on relatively large analytical
62 uncertainties and the resulting inadequate resolution between equilibrium fractionation and
63 kinetic isotope effects.

64 Therefore, to robustly understand how Ca isotopes fractionate during fractional crystallization
65 necessitates high-resolution surveys of a co-genetic and unaltered magma sequence. We targeted
66 the late-Permian alkaline igneous suite of the Øyangen Caldera, Oslo Rift, southern Norway, for
67 a case study that recorded a continuous closed-system fractional crystallization series. Ca-isotope
68 data robustly depict prominent $^{44}\text{Ca}/^{40}\text{Ca}$ variation (~0.53‰) in the evolved felsic magma
69 (trachytic–rhyolitic), contrasting with minimal fractionation (<0.05‰) in the intermediate
70 magma (trachy-andesitic). By comparing isotope data with isotopic modeling, we found that the
71 marked Ca-isotope fractionation is most likely explained by Rayleigh (equilibrium) isotopic
72 fractionation, with a dominant control by feldspar. We also quantified the Ca-isotope
73 fractionation factors of K-feldspar for the first time. The new findings underscore the enhanced
74 power of Ca stable isotopes in tracing magma differentiation and crustal evolution facilitated by
75 our high-precision measurements.



76

77 **Figure 1.** Sampling locations and major element variations of the Øyangen Caldera, Oslo Rift,
 78 Norway. (A) simplified geological map of the late-Permian Øyangen Caldera (ca. 273 Ma). (B)
 79 Major element vs. Th diagrams showing variations throughout fractional crystallization of the
 80 magma. (C) Total Alkali versus Silica classification of the samples.

81 2. Geological settings and samples

82 The Øyangen Caldera in the Oslo Rift developed in the late Permian (ca. 273 Ma, U-Pb thermal
83 ionization mass spectrometry zircon ages) (Corfu and Larsen, 2020) during a prolonged period of
84 rift-related magmatic activity associated with the Oslo Rift from ca. 300–260 Ma (Fig. 1) (Corfu
85 and Dahlgren, 2008; Corfu and Larsen, 2020). The Oslo Rift is located in the foreland of the
86 Variscan Orogen, formed by NW-SE lithospheric extension associated with accumulated
87 tectonic stress during the Laurasia-Gondwana collision (Neumann et al., 2004). It has preserved
88 a series of rift-related sedimentary and igneous rocks, among which the Øyangen Caldera formed
89 in its late-stage development (Fig. 1A) (Neumann et al., 1992; Larsen et al., 2008; Corfu and
90 Larsen, 2020). The basement on both sides of this part of the Oslo Rift consists of high-grade
91 metamorphic rocks (ca. 1.64–1.52 Ga) (Lamminen et al. 2011). This basement is overlain by a
92 few hundred meters to a kilometer of Cambrian to Silurian sediments adjacent to the Øyangen
93 Caldera complex (Fig. 1A). Basaltic lavas of the central volcano marked the onset of Øyangen
94 Caldera magmatism. Caldera collapse followed with the emplacement of ring dykes and central
95 domes and ignimbrite eruptions toward more evolved trachytic–rhyolitic magma compositions
96 (Larsen et al., 2008). For calderas, access to deep-seated magma is assumed to be cut off before
97 the caldera collapse (e.g., Cashman and Giordano, 2014), favoring a closed-system fractional
98 crystallization origin of the igneous suite. Well-preserved remnants of the caldera complex in the
99 area enable comprehensive petrological and geochemical characterization with clear geological
100 context.

101 To constrain the extent of magma evolution, 21 representative samples collected from the
102 Øyangen Caldera were selected for elemental and isotopic analysis, including 2 basanites, 12
103 syenites (8 from coarse-grained ring dykes and 4 from fine-grained central domes), and 7
104 trachytic–rhyolitic ignimbrites (6 trachytes and 1 rhyolite) (Fig. 1A, Table 1). The basanites are
105 mainly comprised of olivine and clinopyroxene with minimal plagioclase. The syenites and
106 trachytic–rhyolitic ignimbrites predominantly consist of feldspar. The ring-dyke syenites contain
107 mostly anorthoclase, while the central-dome syenites and trachytic–rhyolitic ignimbrites contain
108 primarily potassium feldspar. The main-series magma consists of basanites, ring-dyke syenites,
109 and central-dome syenites, complemented by eruptive trachytic–rhyolitic ignimbrites with a
110 more complicated petrogenesis.

111 3. Methods

112 3.1 Sample preparation

113 All whole-rock samples were ground into fine powders, from which we weighed ~50 mg for
114 each to ensure homogeneous bulk compositions. The samples were then processed through
115 standard silicate dissolution (Supplementary Material: Section 1). Major and trace element
116 analyses were performed on a Thermo Scientific iCAP-TQ quadrupole inductively coupled
117 plasma mass spectrometer (ICP-MS) in the Harvard University isotope geochemistry and
118 cosmochemistry laboratory. Dilute HNO₃ (~2%) spiked with 10 parts per billion (ppb) indium,
119 for internal instrumental drift correction, was added into sample aliquots to make final solutions
120 for elemental analysis. Three standard solutions BCR-1, BHVO-1, and AGV-1 were measured to
121 define calibration curves to determine the elemental concentrations of the samples. Major

122 elements of mineral phenocrysts separated from the samples, including clinopyroxene,
123 amphibole, and feldspar, were analyzed by X-ray fluorescence (XRF) at the University of Oslo,
124 Norway.

125 We adapted a modified Ca separation technique following Feng et al. (2018). For calcium-rich
126 samples (CaO wt.% > 1 — basanites and primitive ring-dyke syenites), we loaded sample
127 aliquots containing 40 µg Ca in 4 N HNO₃ onto PFA microcolumns packed with Eichrom DGA
128 spec normal extraction resin (2.4 mm inner diameter, 54 mm height, ~250 µL bed volume). We
129 accelerated the extraction process with a modified Eichrom vacuum box, setting a stable flow
130 rate at ~1mL/5 minutes. Ten bed volumes of 0.1 N HCl (2.5 mL) followed by five bed volumes
131 of 4 N HNO₃ (1.25 mL) were used to clean and condition the column before sample loading. We
132 eluted major elements with a total of 8 mL 4 N HNO₃ and collected pure Ca solutions in 4 mL
133 Milli-Q purified deionized water (for a representative column calibration curve see Fig. S4).
134 Separated Ca solutions were then evaporated to dryness on a hot plate and were redissolved in 2%
135 HNO₃ to make final Ca stock solutions.

136 We found that with very low Ca concentrations [CaO (wt.%) < 1%], separation on the DGA
137 micro-columns often led to impure Ca solutions (Ca purity < 99%), which are not ideal for
138 isotopic measurements with the Nu Sapphire multicollector (MC) ICP-MS due to potential
139 matrix effects. Therefore, to first concentrate Ca in the low-Ca samples (evolved syenites from
140 ring dykes and central domes and trachytic–rhyolitic ignimbrites), they were pre-processed
141 through a 17-cm quartz glass column packed with BioRad AG50W-X8, 100-200 mesh, cation
142 exchange resin eluting with 1.5 N and 2.5 N HCl (method modified from Tera et al., 1970) (for a
143 representative column calibration curve see Fig. S5). A PFA teflon column (4.0 mm inner
144 diameter, 40 mm height, ~500 µL bed volume) packed with Eichrom DGA spec normal
145 extraction resin was used as a second step to purify the Ca, eluting major elements with 2 mL 4N
146 HNO₃ and collecting Ca in 5 mL Milli-Q water. The preliminary separates were then dried and
147 loaded onto the 54 mm PFA teflon microcolumns for final Ca purification. Testing of this
148 method demonstrates that it introduces no additional Ca-isotope fractionation (Supplementary
149 Material: Section 2.1). We tested all separated Ca solutions on our iCAP-TQ quadrupole ICP-
150 MS, ensuring Ca purity [Ca (wt.)/total mass] > 99% for all sample solutions.

151 *3.2 Ca isotope measurements*

152 We measured Ca isotope ratios with a Nu Sapphire MC-ICP-MS (serial no. SP001) in the
153 Harvard University isotope geochemistry and cosmochemistry laboratory. The Nu Sapphire (MC)
154 ICP-MS features a low-energy ion path with a hexapole collision/reaction cell that circumvents
155 the ⁴⁰Ar⁺ interference on mass 40, permitting direct measurement of ⁴⁰Ca relative to other Ca
156 isotopes. We used 2% HNO₃ to dilute purified Ca solutions to ~350 ppb for analysis. An Apex
157 Omega Desolvating Nebulizer introduced the Ca solutions to the plasma torch. After fine-tuning,
158 peak ⁴⁰Ca signal reached up to ~300 V. We implemented a sample-standard bracketing approach
159 to correct for instrumental mass fractionation and internal drift throughout data acquisition, using
160 our in-house laboratory standard, a very high purity Ca solution from Inorganic Ventures (CaIV-
161 1). Each run included 5 repetitive measurements for each sample. We repeated runs for most of
162 the samples on multiple days, obtaining 10 to 20 total measurements. We acquired an average of

163 ~0.022‰ internal precision (two standard errors) for $^{44}\text{Ca}/^{40}\text{Ca}$ measurements (Supplementary
164 Material: Section 2.1).

165 We express stable Ca isotope data using δ -notation:

$$166 \quad \delta^{44/i}\text{Ca} (\text{‰}) = [({}^{44}\text{Ca}/i\text{Ca})_{\text{sample}} / ({}^{44}\text{Ca}/i\text{Ca})_{\text{standard}} - 1] \times 1,000 \quad (1)$$

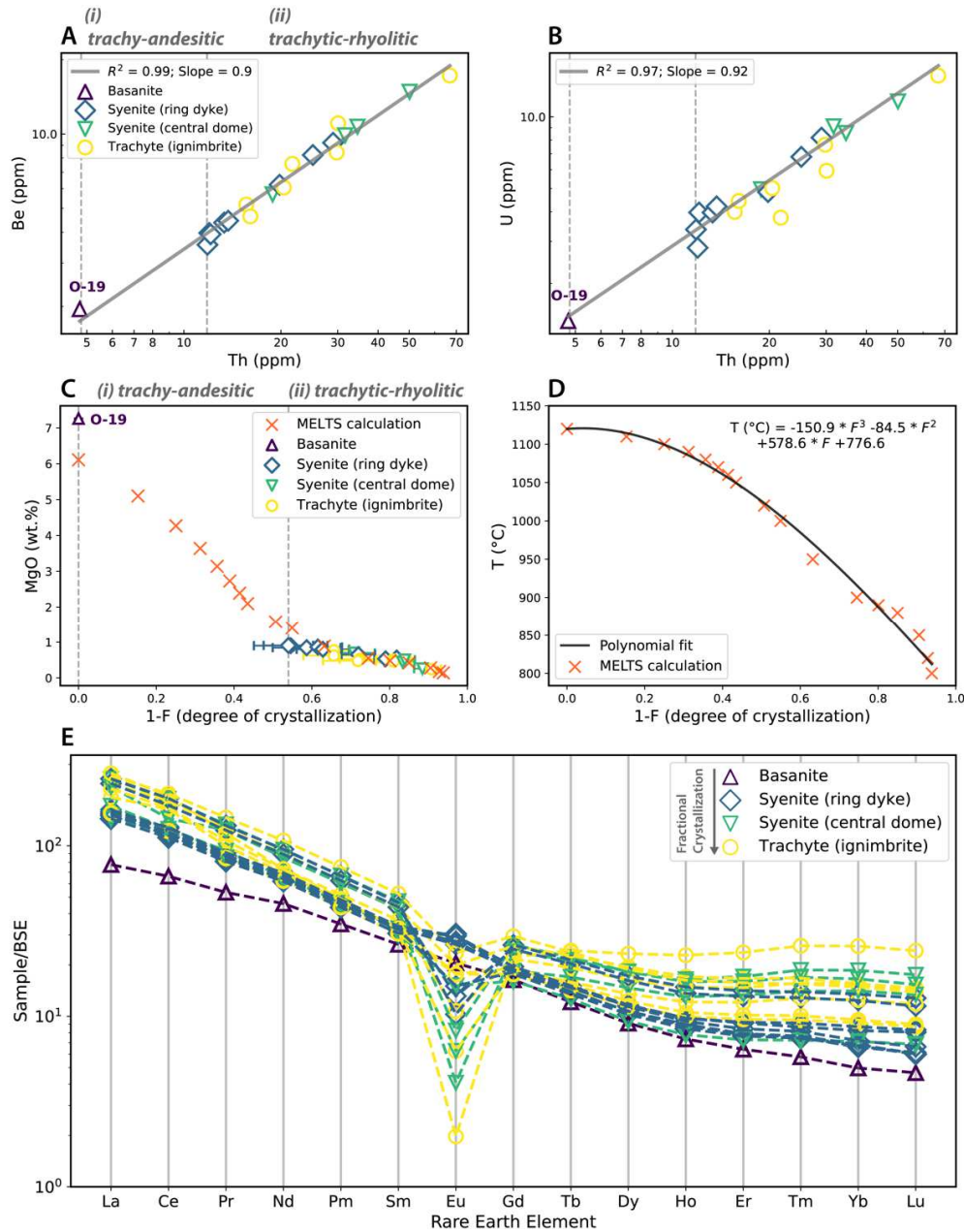
167 where i is the Ca isotope mass 40 or 42. Unless specified as $\delta^{44/40}\text{Ca}_{\text{CaIV}}$, we report $\delta^{44/i}\text{Ca}$ values
168 relative to standard SRM915a. The $\delta^{44/40}\text{Ca}$ value of SRM915a relative to CaIV-1 ($\delta^{44/40}\text{Ca}_{\text{CaIV}}$)
169 has been determined in the lab with external reproducibility of 0.011‰ over the past two years
170 (Fig. S1, Table S4). As such, the minimal uncertainty is neglected when converting $\delta^{44/40}\text{Ca}_{\text{CaIV}}$
171 to $\delta^{44/40}\text{Ca}_{\text{SRM915a}}$. We estimated a ~0.028‰ external reproducibility for the $\delta^{44/40}\text{Ca}$ data. See
172 Supplementary Material: Section 2 for more details on mass spectrometry.

173 4. Results

174 4.1 Major and trace elements

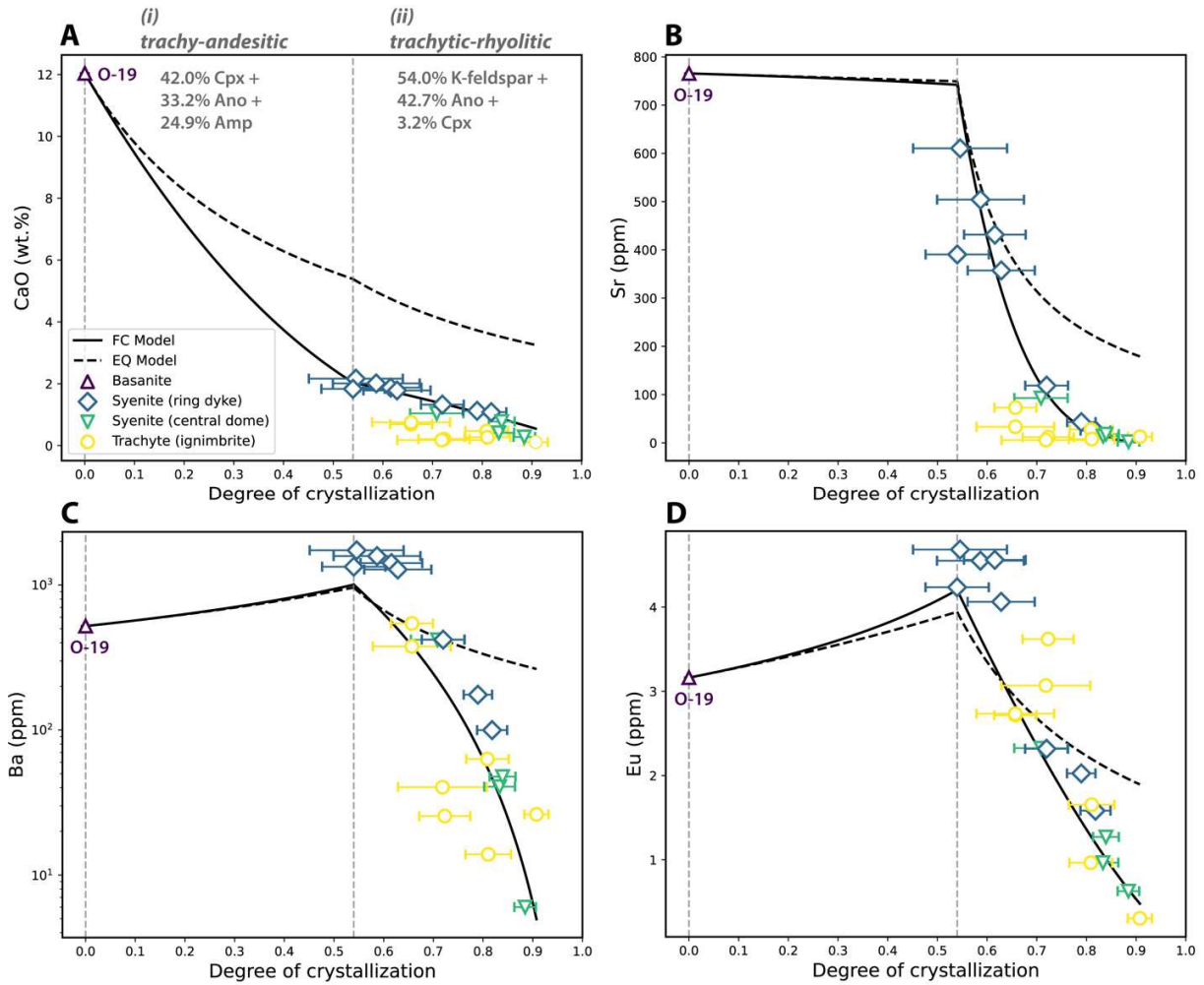
175 Major and trace element data for whole-rock samples are reported in Table S1. We illustrate
176 major element variability relative to Th, a highly incompatible trace element in major rock-
177 forming minerals (partition coefficient, the ratio of concentrations of an element between a
178 mineral and the melt, close to zero, $D^{\text{Th}} \approx 0$) (Allègre et al., 1977) (Fig. 1B). Highly incompatible
179 elements concentrate in the melt as the magma crystallizes because they do not easily fit into the
180 crystal lattices of commonly fractionating minerals. Therefore, highly incompatible elements
181 serve as robust indexes of igneous differentiation. Using major element concentrations, we
182 subdivide the Øyangen Caldera samples into two main crystallization stages – (1) the trachy-
183 andesitic stage, ranging from the evolved basanite (O-19) to the most primitive ring-dyke syenite
184 (O-214) (intermediate stage), and (2) the trachytic–rhyolitic stage, ranging from the most
185 primitive ring-dyke syenite to the most evolved rhyolitic ignimbrite (O-249) (felsic stage) (Fig.
186 1B). As Th concentrates in the residual melt with increasing magma solidification, (1) SiO_2
187 increases while MgO and CaO decrease, (2) Al_2O_3 elevates in the trachy-andesitic melts but
188 starts to decline in the trachytic–rhyolitic melts (3) Na_2O and K_2O remain incompatible until the
189 magma becomes felsic, and (4) there is a gradual depletion of TiO_2 and P_2O_5 and mild variations
190 in Fe_2O_3 and MnO in the felsic stage, reflecting fractionation of accessory minerals like ilmenite,
191 titanomagnetite, and apatite (Fig. 1B). Feldspar compositions are plotted in Fig. 5C (Table S2),
192 indicating that the ring-dyke syenites reflect an anorthoclase component while the central-dome
193 syenites and trachytic–rhyolitic ignimbrites consist of mainly potassium feldspar.

194 Key trace elements in assessing the crystallization sequence are presented in Figs. 2 & 3. Figures
195 2A and 2B show excellent linear correlations between highly incompatible elements in a log-log
196 scale (Be, Th, and U), reflecting nearly constant D throughout the magma crystallization (Allègre
197 et al., 1977). Figure 2E plots the Bulk Silicate Earth (BSE) (McDonough and Sun, 1995)
198 normalized Rare Earth Element (REE) pattern, featuring a growing negative Eu anomaly and
199 increasing concentrations of REEs as the magma differentiates. Variation of CaO, Sr, Ba, and Eu
200 as a function of degree of crystallization are shown in Fig. 3, compared to our elemental
201 modeling results (see text in Discussion 5.1).



202

203 **Figure 2.** Trace element variations and calculation of residual melt fraction (F). (A) & (B)
 204 Highly incompatible elements expressed on a log-log scale exhibit excellent linear correlations
 205 for the main-series samples (basanites, ring-dyke syenites, and central-dome syenites),
 206 suggesting a co-genetic closed-system fractional crystallization sequence. This enables using Be,
 207 U, and Th (Table S1) to independently calculate the residual melt fraction (F). (C) Consistent
 208 variation of MgO and $1-F$ between the MELTS modeling results and our independent estimate of
 209 $1-F$. Our estimates of degree of crystallization ($1-F$) are computed by applying Be, U, and Th
 210 concentrations to equation (4). (D) A polynomial fit to T ($^{\circ}\text{C}$) vs. $1-F$ that solves for magma
 211 crystallization temperature as a function of degree of crystallization. (E) Bulk Silicate Earth
 212 (BSE)-normalized REE patterns (BSE values from McDonough and Sun, 1995).



213

214 **Figure 3.** Trace element variations and equilibrium and fractional crystallization modeling
 215 results. We use the evolved basanite O-19 for the parental magma composition. Mineral partition
 216 coefficients (D) for Sr, Ba, and Eu are from the Geochemical Earth Reference Model (GERM)
 217 Partition Coefficients Database (KdD) (<https://kdd.earthref.org/KdD>). Ano – anorthoclase; Amp
 218 – amphibole; Cpx – clinopyroxene. FC – fractional crystallization; EQ – equilibrium
 219 crystallization.

220 *4.2 Ca-isotope compositions*

221 $\delta^{44/40}\text{Ca}$ versus $\delta^{44/42}\text{Ca}$ is shown in Fig. 4, plotted together with theoretical mass-dependent
 222 fractionation lines under equilibrium and kinetic modes. The total range of $\delta^{44/40}\text{Ca}$ values is 0.23‰
 223 to 0.88‰ (Fig. 4B). Intermediate and felsic samples deviate significantly from the mass
 224 fractionation relationships, with lighter $\delta^{44/40}\text{Ca}$ than is predicted (Fig. 4B). They show increasing
 225 departures from the expected relationship with increasing K/Ca ratios, corresponding to ring-
 226 dyke syenites, central-dome syenites, and trachytic–rhyolitic ignimbrites, respectively (Fig. 4B).
 227 This suggests that the observed displacements are likely due to ^{40}Ca ingrowth via the decay of
 228 ^{40}K to ^{40}Ca (half-life of 1.25 billion years). Using the measured K/Ca ratio for each sample (~2%

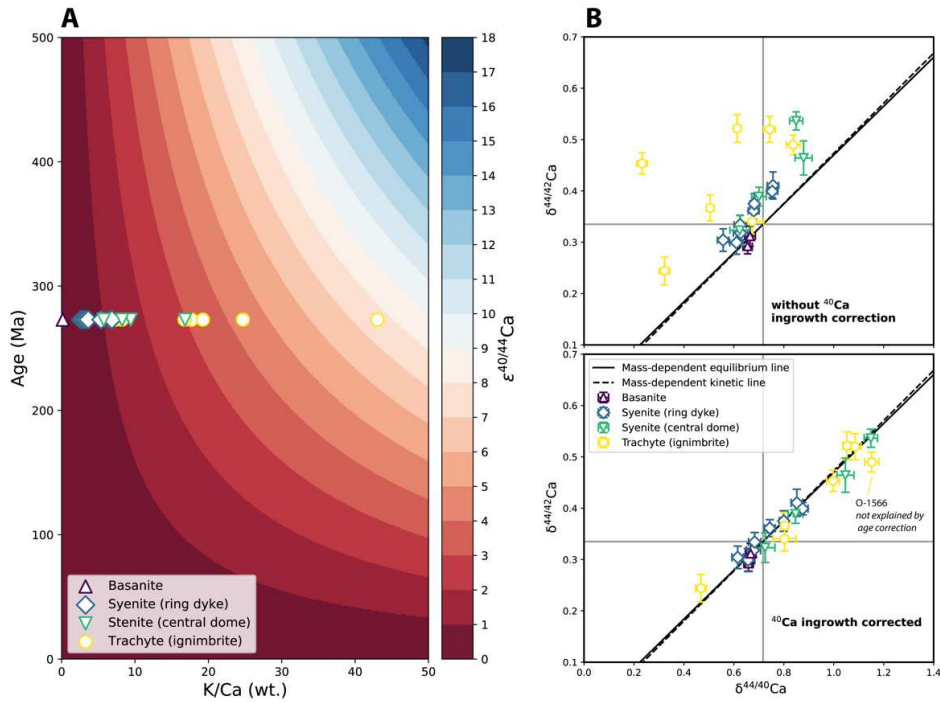
229 external reproducibility) and the age of the rocks (ca. 273 Ma, Corfu and Larsen, 2020), we
 230 quantify the radiogenic excess of ^{40}Ca with the fractionation corrected $^{40}\text{Ca}/^{44}\text{Ca}$ ratio, expressed
 231 as $\epsilon^{40/44}\text{Ca}$ relative to the fractionation corrected terrestrial $^{40}\text{Ca}/^{44}\text{Ca}$ ratio of 47.153 (Russell et
 232 al., 1978), using equation (2):

$$233 \quad \epsilon^{40/44}\text{Ca} = [({}^{40}\text{Ca}/{}^{44}\text{Ca})_{\text{sample (frac-corr)}} / ({}^{40}\text{Ca}/{}^{44}\text{Ca})_{\text{terrestrial (frac-corr)}} - 1] \times 10,000$$

234 (2)

235 $\epsilon^{40/44}\text{Ca}$ is then used to correct for radiogenic ingrowth in the $\delta^{44/40}\text{Ca}$ values of our samples (Fig.
 236 4A) (Supplementary Material: Section 5). After applying the age correction, all samples plot
 237 along the mass fractionation lines within analytical uncertainty except sample O-1566 (Fig. 4B).
 238 Therefore, radiogenic ingrowth of ^{40}Ca is the primary cause of the scatter about the expected
 239 mass-dependent fractionation line.

240 The radiogenic-excess-corrected $\delta^{44/40}\text{Ca}$ data exhibit a total of $\sim 0.68\text{‰}$ variation that ranges
 241 from $0.47 \pm 0.02\text{‰}$ to $1.15 \pm 0.03\text{‰}$ (Table 1). The basanites have similar $\delta^{44/40}\text{Ca}$ values;
 242 $\delta^{44/40}\text{Ca}$ increases systematically from primitive ring-dyke syenites to differentiated central-dome
 243 syenites; while the trachytic–rhyolitic ignimbrites scatter over a large variability (Fig. 4B) (Table
 244 1).



245
 246 **Figure 4.** Ca-isotope data and ^{40}K - ^{40}Ca radiogenic ingrowth correction. (A) $\epsilon^{40/44}\text{Ca}$ as a function
 247 of K/Ca (wt.) and age of the rocks (ca. 273 Ma for the Øyangen Caldera). (B) $\delta^{44/42}\text{Ca}$ vs.
 248 $\delta^{44/40}\text{Ca}$ (relative to standard SRM915a) before and after age correction for ^{40}Ca ingrowth. After
 249 correction, only O-1566 does not fall along the theoretical mass fractionation lines, implying an
 250 isotope composition not accounted for by K-Ca age correction. The mass-dependent equilibrium
 251 line is defined by a slope of 2.0995^{-1} , while the kinetic line has a slope of 2.0483^{-1} (Young et al.,

252 2002). The intercept of the horizontal and vertical grey lines shows the $\delta^{44/40}\text{Ca}$ (0.717‰) and
 253 $\delta^{44/42}\text{Ca}$ (0.335‰) values of CaIV-1 relative to SRM915a, which are close to the values of the
 254 analyzed igneous rocks.

Table 1
 Ca isotope compositions and magmatic context for the samples.

Sample	$^{44}\text{Ca}/^{40}\text{Ca}$				$^{44}\text{Ca}/^{42}\text{Ca}$			CaO (wt.%)	Eu/Eu*	Degree of crystallization (%)	T^* (C)	K/Ca (wt.)	$\epsilon^{40/44}\text{Ca}$	n
	$\delta^{44/40}\text{Ca}_{\text{CaIV}}$ (no corr.)	$\delta^{44/40}\text{Ca}_{\text{SRM915a}}$ (no corr.)	$\delta^{44/40}\text{Ca}_{\text{SRM915a}}$ (corr.)	$\pm 2\text{SE}$	$\delta^{44/42}\text{Ca}_{\text{CaIV}}$	$\delta^{44/42}\text{Ca}_{\text{SRM915a}}$	$\pm 2\text{SE}$							
<i>Basanite</i>														
O-22	-0.062	0.655	0.659	0.019	-0.043	0.292	0.015	11.3	1.01	-	-	0.2	0.04	20
O-19	-0.052	0.665	0.667	0.021	-0.023	0.312	0.020	12.0	0.99	0.0	1120	0.2	0.03	15
<i>Syenite (ring dyke)</i>														
O-214	-0.160	0.557	0.615	0.023	-0.031	0.304	0.022	1.8	1.12	54.0	1010	3.3	0.58	15
O-198	-0.106	0.611	0.657	0.027	-0.036	0.299	0.023	2.2	1.31	54.6	1008	2.6	0.46	15
O-101	-0.090	0.627	0.678	0.028	-0.017	0.318	0.014	2.0	1.22	58.7	991	2.9	0.52	15
O-127	-0.092	0.625	0.683	0.025	-0.001	0.334	0.019	1.9	1.15	61.6	978	3.3	0.58	15
O-11	-0.038	0.679	0.744	0.022	0.026	0.361	0.017	1.8	1.06	62.8	972	3.6	0.65	15
O-50	0.040	0.757	0.852	0.023	0.076	0.411	0.026	1.3	0.62	72.0	929	5.4	0.96	15
O-344	-0.035	0.682	0.800	0.017	0.040	0.375	0.020	1.1	0.40	79.0	893	6.6	1.18	15
O-94	0.036	0.753	0.875	0.022	0.064	0.399	0.012	1.1	0.29	81.8	878	6.8	1.22	15
<i>Syenite (central dome)</i>														
O-8	-0.094	0.623	0.725	0.039	-0.012	0.323	0.029	1.0	0.68	70.8	934	5.7	1.02	15
O-66	0.162	0.879	1.047	0.034	0.129	0.464	0.033	0.4	0.25	83.3	870	9.4	1.67	15
O-171	-0.016	0.701	0.847	0.030	0.054	0.389	0.018	0.8	0.23	83.9	867	8.2	1.46	15
O-3	0.133	0.850	1.149	0.027	0.201	0.536	0.018	0.3	0.13	88.5	842	16.8	2.99	15
<i>Trachytic-rhyolitic ignimbrite</i>														
O-430	-0.044	0.673	0.803	0.047	0.006	0.341	0.024	0.8	0.70	65.7	959	7.3	1.30	15
O-586	-0.395	0.322	0.468	0.022	-0.091	0.244	0.027	0.7	0.76	65.7	959	8.2	1.46	10
O-33	-0.103	0.614	1.053	0.017	0.187	0.522	0.027	0.2	0.60	71.8	930	24.7	4.39	15
O-1566	0.121	0.838	1.152	0.028	0.155	0.490	0.019	0.2	0.60	72.3	927	17.7	3.15	10
O-145	-0.212	0.505	0.803	0.017	0.032	0.367	0.025	0.5	0.25	80.9	883	16.8	2.98	15
O-589	0.026	0.743	1.085	0.024	0.185	0.520	0.025	0.3	0.38	81.0	882	19.3	3.42	15
O-249	-0.485	0.232	0.997	0.026	0.118	0.453	0.021	0.1	0.07	90.7	829	43.0	7.65	15

Notes:
 (corr.)/(no corr.) — corrected/not corrected for radiogenic excess of ^{40}Ca . n is the number of replicate measurements. Crystallization temperature, T^* (C), is determined from the fitting of T^* (C) as a function of degree of crystallization (Fig. 2D). 2SE represents two standard errors of the means. An about 2% error in the measured K/Ca (wt.) has been propagated to obtain the 2SE of $\delta^{44/40}\text{Ca}$ data.

256 5. Discussion

257 5.1 Co-genetic fractional crystallization of the Øyangen Caldera

258 Major element variations as a function of Th are consistent with a fractional crystallization origin
 259 for the Øyangen Caldera (Fig. 1B), in which the intermediate stage is dominated by fractionation
 260 of clinopyroxene + amphibole + plagioclase and the felsic stage is controlled by fractionation of
 261 alkali feldspar + clinopyroxene. Such a change in the crystallizing mineral assemblage agrees
 262 with the mineral analyses (Table S2).

263 Correlations between highly incompatible elements also support a fractional crystallization
 264 sequence of the Øyangen Caldera. Excellent linear relationships ($R^2 > 0.9$) and slopes ≈ 1
 265 between Be, Th, and U in log-log plots (Fig. 2A&B) are distinctive manifestations of a co-
 266 genetic magma series formed by closed-system fractional crystallization (Allègre et al., 1977).
 267 The evolution of elemental concentrations following fractional crystallization gives:

$$268 \quad \frac{C_m^i}{C_T^i} = F^{(D^i-1)}$$

269 (3)

270 Where C_m^i is the concentration of element i in the remaining melt; C_T^i is the concentration of i in
 271 the primary magma; D^i is the partition coefficient; F is the residual melt fraction. For a highly
 272 incompatible element ($D \approx 0$), F associated with a sample can be calculated using the elemental
 273 concentration in the parental magma (C_T^i) and in each individual sample (Allègre et al., 1977):

274
275

$$F = C_T^i / C_{sample}^i$$

(4)

276 Here we used the evolved basanite O-19 for the parental magma composition (C_T^i) to study the
277 intermediate and felsic magmatic differentiation. We computed F independently using Be, U, and
278 Th and averaged the results to obtain a mean F -value, which we converted to the degree of
279 crystallization, defined here as $1-F$ (Table 1, Table S1). We also modeled the liquid line of
280 descent of the Øyangen Caldera using the Rhyolite-MELTS thermodynamic program (Gualda et
281 al., 2012). For MELTS modeling, we implemented a fractional crystallization model and used O-
282 22 (the most primitive basanite) as the primary magma composition (Supplementary Material:
283 Section 3). Figure 2C shows the high consistency of MgO vs. $1-F$ between the MELTS
284 calculation and our estimate of $1-F$ using highly incompatible elements, substantiating that the
285 samples document a closed-system fractional crystallization sequence. Therefore, the
286 crystallization temperatures of the samples can be constrained by fitting temperature as a
287 function of F from the MELTS results (Fig. 2D).

288 To estimate the proportions of fractionating minerals in individual crystallization stages, we
289 implemented a weighted-least-squares method (Wright and Doherty, 1970) with our measured
290 major element concentrations for mineral phenocrysts (for results see Fig. 3A and Table S3)
291 (Supplementary Material: Section 4). We also determined the mineral proportions for the
292 crystallization stages of the syenites from ring dykes and central domes independently (Fig. 5D).
293 For robustness, we tested our crystallization model with trace element modeling assuming
294 fractional crystallization [equation (3)] and compare it with equilibrium crystallization, a
295 presumed less likely explanation for the caldera magma chamber (e.g., Cashman and Giordano,
296 2014, Gavrilenko et al., 2016):

297
298

$$\frac{C_m^i}{C_T^i} = [F + D^i (1 - F)]^{-1}$$

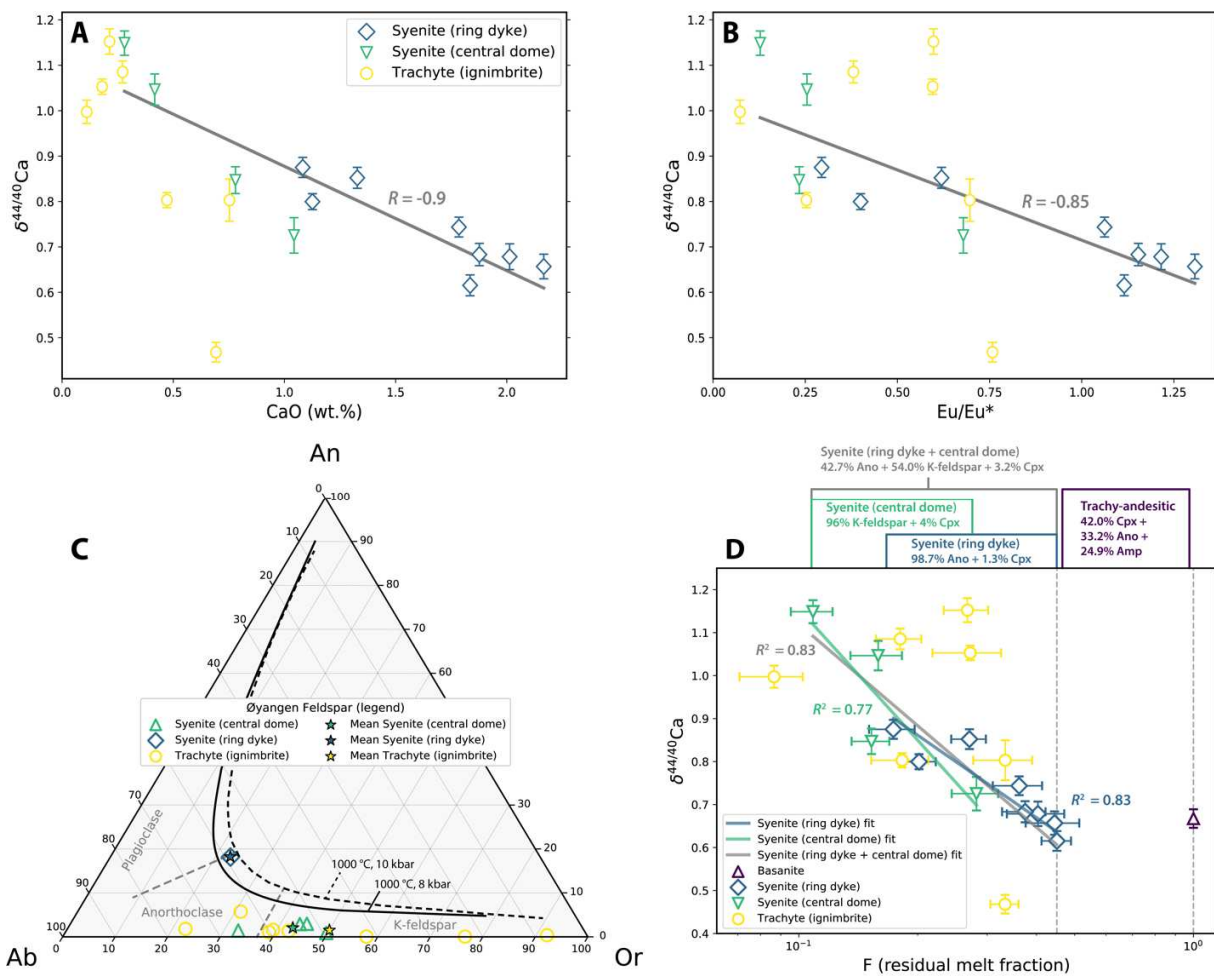
(5)

299 Using the calculated mineral proportions and mineral partition coefficients (Table S3, from the
300 Geochemical Earth Reference Model Partition Coefficients Database,
301 <https://kdd.earthref.org/KdD>), we modeled trace elemental variations of Sr, Ba, and Eu in the
302 melt (Fig. 3 B–D). The modeled evolution of CaO is also plotted versus our data (Fig. 3A).
303 Comparing data and modeling results yields remarkable agreement between the major and trace
304 element systematics and our fractional crystallization model. In particular, the fractional
305 crystallization modeling matches the characteristic depletions of Sr, Ba, and Eu up to extreme
306 degrees of solidification (54–91%), which are all diagnostic features of feldspar fractionation. In
307 addition, the extremely low concentrations of Sr, Ba, and Eu in the late stages of differentiation
308 make them sensitive tracers of magma mixing. For example, the extensive depletion of Sr puts
309 strong constraints on the extent of contamination as the possible contaminants have much higher
310 Sr concentrations (~250 ppm for the Precambrian basement and ~700 ppm for the Cambrian to
311 Silurian sediments) (Neumann et al., 1985). Contaminating the differentiating magma with these
312 rocks would not reproduce the extremely-depleted Sr concentrations that are observed. Together,
313 the consistent and systematic and decrease in Sr, Ba, and Eu, especially for the main-series
314 magma, precludes magma mixing during magma differentiation.

315 To further test open-system behavior, we have modeled elemental variations expected for open-
316 magma crystallization (DePaolo, 1981) to compare with our data. The elemental variations of
317 CaO (a representative compatible element) and Th (a representative incompatible element),
318 including both the main-series syenites and trachytic–rhyolitic ignimbrites, agree best with the
319 modeled closed-system crystallization (Fig. S8). The observed elemental variations also do not
320 display the diagnostic features predicted for open-magma crystallization: limited depletion of
321 compatible elements (such as Ca) and continuous enrichment in incompatible elements (such as
322 Th) (O’Hara, 1977, DePaolo, 1981) (Fig. S8). Therefore, these comparisons conclude that the
323 Øyangen samples document a very limited extent of magma replenishment during magma
324 differentiation.

325 Within the felsic stage, trachytic–rhyolitic ignimbrites display a nuanced but discernable
326 deviation from the evolution of syenites from ring dykes and central domes, manifesting in both
327 major element (e.g., Na₂O, K₂O, CaO, MnO) and trace element (e.g., Sr, Ba) variations (Fig. 1B,
328 Fig. 3). Also, the trachytic–rhyolitic ignimbrites generally have a larger spread in elemental
329 concentrations. Such differences likely result from the complex source materials incorporated in
330 the formation of eruptive ignimbrites, in contrast to the intrusive main series of magma.

331 In summary, major and trace element variations and modeling resolve a co-genetic fractional
332 crystallization sequence recorded in the samples, of which feldspar dominates the late-stage Ca
333 budget. Affirmation of the magmatic history enables us to directly probe Ca-isotope systematics
334 during magmatic differentiation.



335

336 **Figure 5.** Ca-isotope variations with feldspar fractionation. (A) & (B) $\delta^{44/40}\text{Ca}$ vs. CaO (wt.%)
 337 and $\delta^{44/40}\text{Ca}$ vs. Eu/Eu* for the felsic-stage magma. Correlation coefficients (R) are determined
 338 using the main-series syenite samples from ring dykes and central domes. (C) Anorthite (An) –
 339 Albite (Ab) – Orthoclase (Or) ternary diagram illustrating feldspar compositions for our samples.
 340 Curves show the calculated miscibility gaps for 1,000 °C following Yoshimura et al. (2008). The
 341 ca. 1,000 °C crystallization temperature for the anorthoclase in the syenites from ring dykes is
 342 broadly consistent with the MELTS calculation. (D) $\delta^{44/40}\text{Ca}$ as a function of $\ln(F)$, where a
 343 linear relationship [slope = $1,000D(\alpha-1)$] is expected for Rayleigh isotopic fractionation (see
 344 text). The best-fit slopes yield bulk α , from which α of feldspar can be disentangled and
 345 estimated. Uncertainties on the data are two standard errors (2SE). Ano – anorthoclase; Amp –
 346 amphibole; Cpx – clinopyroxene.

347 5.2 Rayleigh (equilibrium) isotopic fractionation of the main-series samples

348 With the fractional crystallization sequence established above, we assess the mechanism for the
 349 observed Ca-isotope variations in our samples. The strong correlations between $\delta^{44/40}\text{Ca}$, CaO,
 350 and Eu/Eu* for the main-series syenite samples (Fig. 5) substantiates that the Ca-isotope changes
 351 are best explained by feldspar fractionation during crystallization. Weak to no correlations
 352 between $\delta^{44/40}\text{Ca}$, CaO, and Eu/Eu* of the trachytic–rhyolitic ignimbrites (Fig. 5) align with their
 353 complex petrogenetic origins. Thereby, the Ca isotope data of trachytic–rhyolitic ignimbrites are
 354 not prioritized for interpretations in the context of magmatic differentiation.

355 During magma crystallization, mass-dependent equilibrium and kinetic isotopic fractionation
 356 could both be important (Watson and Müller, 2009; Antonelli et al., 2019a and 2019b).
 357 Significant $\delta^{44/40}\text{Ca}$ variations (up to $\sim 0.2\text{‰}$) within melt compositions have been mostly
 358 observed from volcanic units (Zhu et al., 2021). Fractionation greater than $\sim 0.2\text{‰}$ was mainly
 359 ascribed to kinetic isotopic effects via Ca diffusion during rapid feldspar growth (Antonelli et al.,
 360 2019b; Zhu et al., 2021). The main series of the Øyangen samples, consisting of intrusive
 361 syenites from ring dykes and central domes, displays a total $\delta^{44/40}\text{Ca}$ change of $\sim 0.53\text{‰}$, so far,
 362 the largest systematic variations confirmed for a well-preserved magma series. Importantly, this
 363 is the first pronounced Ca-isotope variation discovered from a sequence of igneous intrusions
 364 instead of volcanics. Clarifying the fractionation mechanism of the Øyangen samples is vital for
 365 our fundamental understanding of Ca isotopic variability among diverse igneous origins and
 366 conditions, which ultimately defines the power of Ca-isotopes as a tracer of magmatic
 367 differentiation.

368 The slow crystallization rates of intrusive rocks are most compatible with fractionation closer to
 369 expected equilibrium (Watson and Müller, 2009, Antonelli et al., 2019a). This can be further
 370 tested by comparing our Ca-isotope data with the Rayleigh equilibrium fractionation model,
 371 which gives:

$$372 \quad \delta^{44/40}\text{Ca}_{melt} = (1,000 + \delta_T^{44/40}\text{Ca}) f^{(\alpha^{44/40}\text{Ca}-1)} - 1,000$$

373 (6)

374 Expressing $\delta^{44/40}\text{Ca}$ as a function of $\ln(F)$, equation (6) becomes:

$$375 \quad \delta^{44/40}\text{Ca}_{melt} = \delta_T^{44/40}\text{Ca} + 1,000D(\alpha^{44/40}\text{Ca} - 1)\ln(F) \quad (7)$$

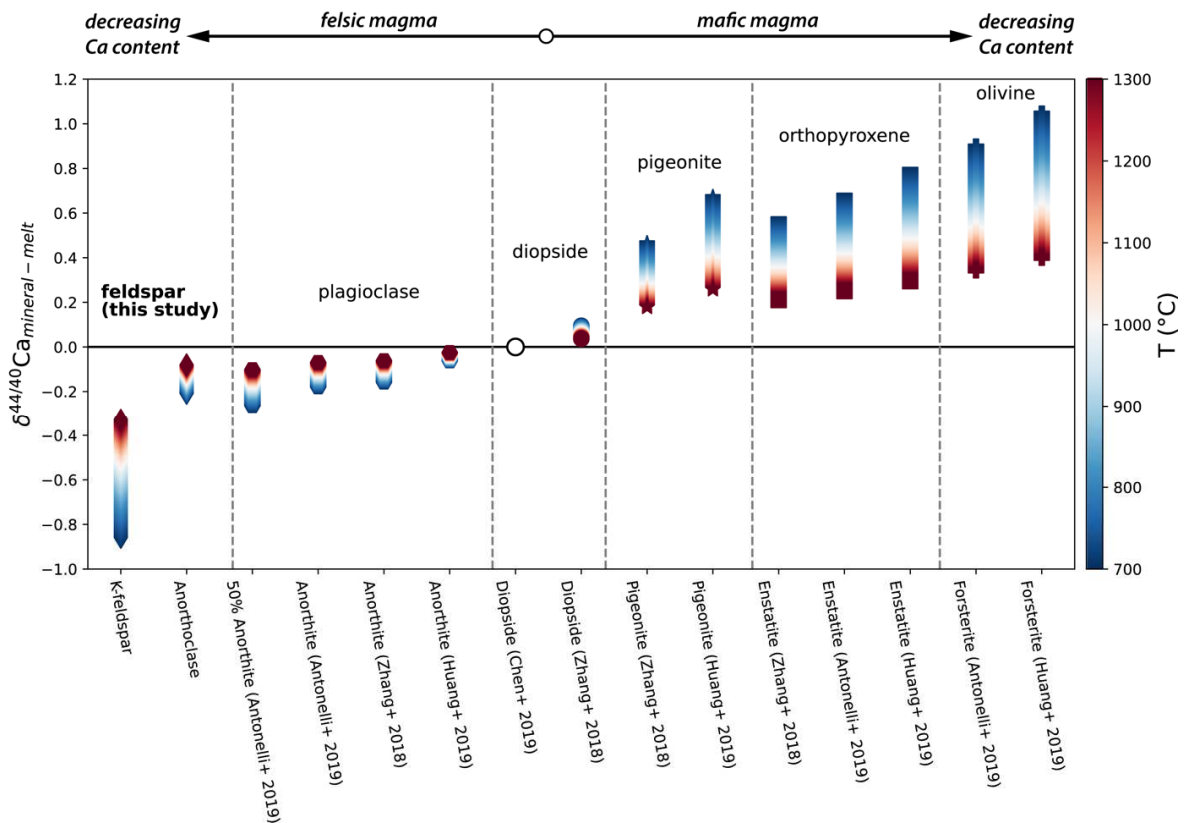
376 where $\delta^{44/40}\text{Ca}_{melt}$ is the evolution of the Ca-isotope ratio in the melt; $\delta_T^{44/40}\text{Ca}$ is the initial
 377 isotopic composition; $f (= F^D)$ is the mass fraction of the reference isotope (^{40}Ca) in the melt;
 378 $\alpha^{44/40}\text{Ca}$ is the bulk fractionation factor of the fractionating mineral assemblage [$\alpha^{44/40}\text{Ca} =$
 379 $(^{44}\text{Ca}/^{40}\text{Ca}_{\text{solid}})/(^{44}\text{Ca}/^{40}\text{Ca}_{\text{melt}})$]. The $^{44}\text{Ca}/^{40}\text{Ca}$ evolution of the instantaneous cumulates follows as:

$$380 \quad \delta^{44/40}\text{Ca}_{cum} = \delta^{44/40}\text{Ca}_{melt} + 1,000\ln(\alpha^{44/40}\text{Ca})$$

381 (8)

382 Equation (7) expresses a linear relationship between $\delta^{44/40}\text{Ca}_{melt}$ and $\ln(F)$, whose slope is
 383 given by $1,000D(\alpha-1)$. This approach can test whether Rayleigh fractionation describes the
 384 observed isotopic changes and allows for application of linear regression to define the best-fit
 385 bulk $\alpha^{44/40}\text{Ca}$.

386 We present measured $\delta^{44/40}\text{Ca}$ versus $\ln(F)$ in Fig. 5D. Linear regressions yield high correlation
 387 coefficients ($R^2 = 0.83$, $N = 12$) for all main series samples of the felsic stage, as well as for
 388 independent fittings for the syenites from ring dykes ($R^2 = 0.83$, $N = 8$) and the central dome
 389 samples ($R^2 = 0.77$, $N = 4$). This demonstrates that the Ca-isotope changes agree well with
 390 Rayleigh fractionation models throughout magma solidification. In more detail, we observe no
 391 systematic $\delta^{44/40}\text{Ca}$ offset between the fine-grained syenites from central domes and coarse-
 392 grained syenites from ring dykes along the main evolution trend (Fig. 5D). This implies no
 393 discernable signatures of disequilibrium effects induced by variable rates of crystal precipitation,
 394 which otherwise could result in separate fractionation behaviors between the two types of melts.
 395 For instance, if kinetic effects played a considerable role during crystallization, the rapid-cooling
 396 central-dome syenites could have generated a systematic shift from the $\delta^{44/40}\text{Ca}$ evolution of the
 397 slow-cooling ring-dyke syenites, assuming that the kinetic Ca-isotope fractionation is larger for
 398 faster crystallizing feldspar (Antonelli et al., 2019a). Therefore, the Ca-isotope results for the
 399 main series favor an equilibrium fractionation mechanism, although the possible involvement of
 400 minor kinetic effects cannot be excluded. The substantial deviations of the $\delta^{44/40}\text{Ca}$ values of the
 401 trachytic–rhyolitic ignimbrites from the mean trend of the melt (Fig. 5D) might reflect the
 402 complex and heterogeneous nature of their building materials.



403

404 **Figure 6.** Compilation of mineral–melt $^{44}\text{Ca}/^{40}\text{Ca}$ isotopic fractionation factors of major rock-
405 forming minerals in the Earth’s crust, determined in this study and from the literature.

406 5.3 Isotopic fractionation factors and Ca-isotope evolution

407 Considering that, for systems defined by Rayleigh fractionation, the slope in a plot of $\delta^{44/40}\text{Ca}$
 408 versus $\ln(F)$ equals $1,000D(\alpha-1)$, inversion of the slopes can yield accurate estimations of bulk
 409 $\alpha^{44/40}\text{Ca}$. Using a weighted-least-squares method (Williamson, 1968), we compute the best-fit
 410 slopes for (1) the syenite samples from ring dykes, (2) the syenite samples from central domes,
 411 and (3) the entire felsic stage containing both sample types. A significant difference is resolved
 412 between the slopes of the ring dyke samples and the central dome samples (Fig. 5D), suggesting
 413 considerable changes in bulk $\alpha^{44/40}\text{Ca}$ with the varying mineral compositions and proportions.
 414 We take the mean temperature for each crystallizing assemblage to account for the temperature-
 415 dependence of fractionation factors [$\alpha \sim (1/T)^2$] (e.g., the mean T is 1,217 K for the syenite
 416 samples from ring dykes that span between 1,151 K to 1,284 K) (Fig. 2D) (Table 1). The
 417 corresponding bulk $\alpha^{44/40}\text{Ca}$ at 1,000 K, a reference temperature, is then calculated from
 418 $\alpha^{44/40}\text{Ca}_{(T)}$ using:

$$419 \quad \alpha^{44/40}\text{Ca}_{(T)} - 1 = (\alpha^{44/40}\text{Ca}_{(1,000)} - 1) / \left(\frac{T}{1,000}\right)^2$$

420 (9)

421 Because diopside is the only major Ca-bearing mineral other than feldspar in both the ring-dyke
 422 and central-dome syenite samples, we can determine the $\alpha^{44/40}\text{Ca}$ for feldspar by subtracting the
 423 contribution of $\alpha^{44/40}\text{Ca}_{\text{diopside-melt}}$ from the bulk $\alpha^{44/40}\text{Ca}$. Adopting $\alpha^{44/40}\text{Ca}_{\text{diopside-melt}} = 1.00009 \pm$
 424 0.00007 at 1,000 K from Zhang et al. (2018), $\alpha^{44/40}\text{Ca}_{\text{anorthoclase-melt}}$ and $\alpha^{44/40}\text{Ca}_{\text{K-feldspar-melt}}$ are
 425 disentangled from the ring dyke and central dome samples, respectively (for results see Table 2)
 426 (Supplementary Material: Section 6). Our calculated mineral-melt fractionation factor for the
 427 whole felsic stage, 0.999713 ± 0.000036 (two standard errors) (Table S3), agrees within error
 428 with the mineral-melt fractionation factor obtained by the regression method ($0.999718 \pm$
 429 0.000039), demonstrating the consistency of the $\alpha^{44/40}\text{Ca}_{\text{mineral-melt}}$ estimates.

430 We synthesized the $\alpha^{44/40}\text{Ca}$ estimations for feldspar determined in our study with those for
 431 major rock-forming minerals of Earth's crust from the literature (Fig. 6, Table 2). We expressed
 432 the $^{44}\text{Ca}/^{40}\text{Ca}$ fractionation between minerals and melts as $\delta^{44/40}\text{Ca}_{\text{mineral-melt}} =$
 433 $1,000(\alpha^{44/40}\text{Ca}_{\text{mineral-melt}} - 1)$. Inter-mineral fractionation originally reported as $\delta^{44/40}\text{Ca}_{\text{mineral-}}$
 434 diopside from the literature are converted to $\delta^{44/40}\text{Ca}_{\text{mineral-melt}}$ assuming $\delta^{44/40}\text{Ca}_{\text{diopside-melt}} = 0.09 \pm$
 435 0.07‰ (Zhang et al., 2018). $\delta^{44/40}\text{Ca}_{\text{anorthoclase-melt}}$ from our study exhibits similar fractionation
 436 effects to plagioclase. K-feldspar reveals the most negative $\delta^{44/40}\text{Ca}$ value relative to the melt
 437 discovered so far ($-0.81 \pm 0.10\text{‰}$ at 1,000 K). Ca-isotope analyses of mineral phenocrysts
 438 (Antonelli et al., 2019a) also imply that K-feldspar may have the lightest Ca-isotope signature
 439 among common rock-forming minerals (up to $\delta^{44/40}\text{Ca} = -2\text{‰}$ relative to BSE), broadly
 440 consistent with our results. An overall trend shows that more Ca-depleted minerals bear larger
 441 fractionation effects (Fig. 6). Such a Ca-concentration effect has been predicted by experiments
 442 and first-principles calculations for minerals mainly with positive $\delta^{44/40}\text{Ca}_{\text{mineral-diopside}}$, including
 443 olivine, orthopyroxene, pigeonite, and garnet (Feng et al., 2014; Wang et al., 2017; Huang et al.,
 444 2019, Li et al., 2022). This is primarily an artifact of the length of the Ca-O bond, where heavy
 445 Ca-isotopes (e.g., ^{44}Ca) have a preference for shorter, stiffer bonds. Substituting Ca into crystal
 446 lattices generally increases the length of the Ca-O bond, leading to less-pronounced
 447 fractionations between minerals and melt for minerals enriched in Ca (e.g., Feng et al., 2014;

448 Wang et al., 2017; Huang et al., 2019, Antonelli and Simon, 2020, Li et al., 2022). A possible
449 Ca-concentration effect has been postulated for feldspar with negative $\delta^{44/40}\text{Ca}_{\text{mineral-diopside}}$ from
450 first-principles estimates (lighter $^{44}\text{Ca}/^{40}\text{Ca}$ with decreasing anorthite content, Antonelli et al.,
451 2019a); our data provide the first evidence for this effect in a continuous natural magma
452 sequence.

453 We reconstruct the Ca-isotope evolution of the Øyangen Caldera using Rayleigh fractionation
454 [equation (6) & (8)], accounting for propagated errors surrounding the initial isotopic
455 composition (sample O-19) and temperature-dependent fractionation factors with a Monte Carlo
456 model that we developed (Supplementary Material: Section 7) (Fig. 7, Table S3). We
457 implemented Monte Carlo modeling for (1) measured $\delta^{44/40}\text{Ca}$ (corrected for ingrowth of
458 radiogenic ^{40}Ca) (Fig. 7 A) and (2) $\delta^{44/40}\text{Ca}$ calculated from measured $\delta^{44/42}\text{Ca}$, assuming a mass-
459 dependent fractionation relationship ($\delta^{44/40}\text{Ca} \approx 2.0483 * \delta^{44/42}\text{Ca}$, Young et al., 2002) (Fig. 7B).
460 Both models yield similar results (Fig. 7). The $\delta^{44/40}\text{Ca}$ value of the parental magma ($0.67 \pm$
461 0.02‰) is similar to the typically low average $\delta^{44/40}\text{Ca}$ values of alkaline igneous rocks including
462 ocean island basalts (from $\sim 0.70\text{‰}$ to $\sim 0.85\text{‰}$) (Eriksen and Jacobsen, 2022). Forward modeling
463 of $\delta^{44/40}\text{Ca}$ yields high correspondence with the observed Ca-isotope variability throughout the
464 whole sequence (Fig. 7). Most of the main-series syenite samples and part of the trachytic-
465 rhyolitic ignimbrites overlap the modeled melt curve within the 95% confidence envelope.

466 Our data and modeling corroborate that no discernable $\delta^{44/40}\text{Ca}$ fractionation ($< 0.05\text{‰}$) is
467 expected in an intermediate crystallization sequence, as the isotopic effects of mafic minerals
468 (including clinopyroxene and amphibole) and feldspar nearly cancel out each other. This is
469 consistent with Ca-isotope measurements from the basalt to dacite sequence in the Kilauea Iki
470 lava lake, Hawaii ($< 0.07\text{‰}$ change, Zhang et al., 2018) and from the basaltic andesite to andesite
471 in the eastern Manus Basin (Zhu et al., 2021). Throughout the felsic stage, the $\sim 0.53\text{‰}$ $\delta^{44/40}\text{Ca}$
472 fractionation found in both the intrusions and the volcanics highlights the capacity of Ca-isotopes
473 as a sensitive tracer of igneous fractionation, calling for tests in other magma types and tectonic
474 environments. The discoveries invoke new applications of Ca isotopes in diverse topics
475 surrounding magmatic history at various spatial and temporal scales.

Table 2

Ca isotopic fractionation factors for rock-forming minerals of Earth's crust.

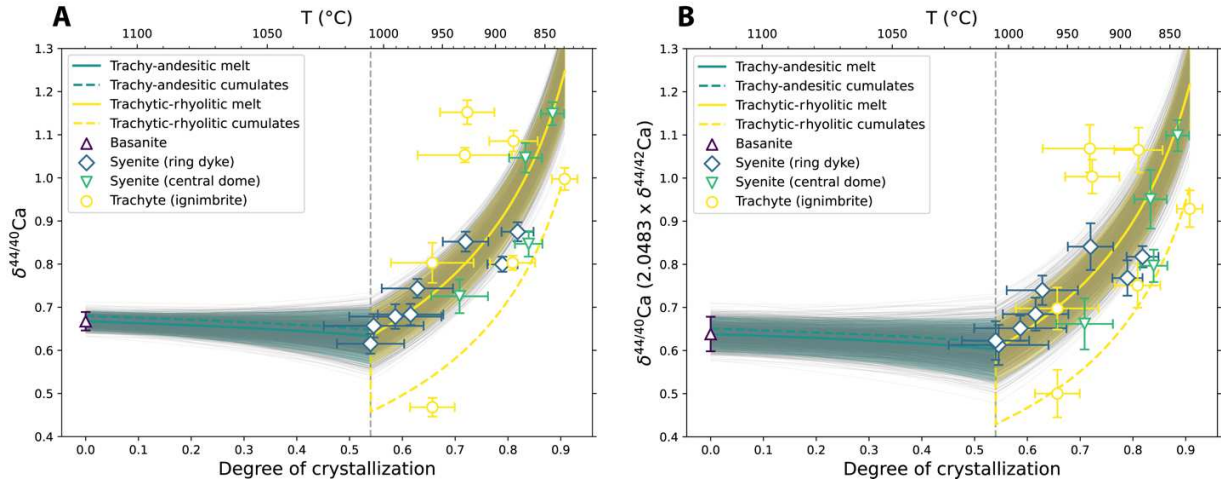
Mineral	$\delta^{44/40}\text{C}_{\text{mineral-melt}}$	2SE (2SD)	$\alpha^{44/40}\text{C}_{\text{mineral-melt}}$	Methods	References
Feldspar					
K-feldspar	-0.81	0.10	0.999187	Data regression	This study
Anorthoclase	-0.20	0.04	0.999803	Data regression	This study
50% Anorthite	-0.25	-	0.999750	First-principles calculation	Antonelli et al. (2019a)
Anorthite	-0.17	-	0.999830	First-principles calculation	Antonelli et al. (2019a)
Anorthite	-0.15	0.08	0.999850	Data regression	Zhang et al. (2018)
Anorthite	-0.06	-	0.999940	First-principles calculation	Huang et al. (2019)
Clinopyroxene					
Diopside	0	-	1.000000	Data interpretation	Chen et al. (2019)
Diopside	0.09	0.07	1.000090	Data regression	Zhang et al. (2018)
Pigeonite	0.44	0.13	1.000440	Data regression	Zhang et al. (2018)
Pigeonite	0.64	-	1.000636	First-principles calculation	Huang et al. (2019)
Orthopyroxene					
Enstatite	0.52	0.1	1.00052	Data regression	Zhang et al. (2018)
Enstatite	0.62	-	1.000620	First-principles calculation	Antonelli et al. (2019a)
Enstatite	0.73	-	1.000730	First-principles calculation	Huang et al. (2019)
Olivine					
Forsterite	0.85	-	1.000850	First-principles calculation	Antonelli et al. (2019a)
Forsterite	0.99	-	1.000990	First-principles calculation	Huang et al. (2019)

Notes :

Isotopic fractionation effects are determined for 1,000 K.

2SE -- two standard errors; 2SD -- two standard deviations.

476



477

478 **Figure 7.** Ca-isotope evolution of the Øyangen Caldera. (A) & (B) $\delta^{44/40}\text{Ca}$ vs. degree of
 479 crystallization. $\delta^{44/40}\text{Ca}$ in (A) are after correction for ^{40}Ca radiogenic ingrowth; $\delta^{44/40}\text{Ca}$ in (B)
 480 are calculated from $\delta^{44/42}\text{Ca}$ assuming a theoretical mass-dependent fractionation relationship.
 481 Isotopic evolution is modeled using Rayleigh fractionation with a Monte Carlo approach
 482 (Supplementary Material: Section 7). For clarity of the figure, fine grey curves show the first
 483 2,000 times out of all 10,000 simulations. Colored solid and dashed curves represent the mean
 484 $\delta^{44/40}\text{Ca}$ compositions of the melt and cumulates, respectively. Colored fields bound the 95%
 485 confidence intervals of our melt model. Uncertainties on the Ca-isotope data are two standard
 486 errors (2SE).

487 5.4 Implications for planetary differentiation

488 Recognizing the prominent feldspar isotopic effects augments the application of Ca-isotopes in
489 studying planet-scale differentiation. Recently, progress has been made in modeling the Ca-
490 isotope evolution throughout the crystallization of the early lunar magma ocean (LMO).
491 Modeling has predicted a decrease in $\delta^{44/40}\text{Ca}$ in the first ~80% of the LMO solidification
492 dominated by olivine and orthopyroxene, followed by an increase in the late stages (~0.05‰)
493 controlled by plagioclase, clinopyroxene, and orthopyroxene (Huang et al., 2019). Using a
494 similar LMO crystallization model and the same set of inter-mineral fractionation factors,
495 however, Klaver et al. (2021) modeled monotonically decreasing $\delta^{44/40}\text{Ca}$ throughout the LMO
496 crystallization. Conflicting results trace two primary causes. First, a systematic offset between
497 their assumptions of mineral-melt fractionations — Huang et al. (2019) assumed $\delta^{44/40}\text{Ca}_{\text{diopside-}}$
498 $\text{melt} = 0 \pm 0.05 \text{‰}$ and Klaver et al. (2021) used $\delta^{44/40}\text{Ca}_{\text{diopside-}}$
499 $\text{melt} = 0.09 \pm 0.07 \text{‰}$ following Zhang et al. (2018). Second, use of a comparatively small $\delta^{44/40}\text{Ca}_{\text{plagioclase-}}$
500 diopside (-0.15‰ at 1,000 K) in both studies. Our resolved $\delta^{44/40}\text{Ca}_{\text{anorthoclase-}}$
501 diopside agrees better with the $\delta^{44/40}\text{Ca}_{\text{anorthite-}}$
502 diopside estimated from Zhang et al. (2018) and Antonelli et al. (2019a) (Table 2), which
503 collectively suggests a value ranging from -0.34‰ to -0.24‰ (at 1,000 K), a more probable
504 estimation for $\delta^{44/40}\text{Ca}_{\text{plagioclase-}}$
505 diopside . Using this larger $\delta^{44/40}\text{Ca}_{\text{plagioclase-}}$
506 diopside would alleviate the discrepancy between models under mildly different assumptions of mineral-melt fractionation.
507 Additionally, the more negative $\delta^{44/40}\text{Ca}_{\text{plagioclase-}}$
508 melt predicts greater variations in $\delta^{44/40}\text{Ca}$ of the LMO approaching its final crystallization and larger fractionation between the magma, sinking cumulates, and the floating anorthite crust, a prediction that is testable in subsequent investigations.

509 Although relatively new to the application of planetary differentiation, Ca-isotopes carry a
510 unique advantage and potential. Other non-traditional stable isotope systematics, including K,
511 Mg, Si, and Fe, are slightly volatile to moderately volatile and prone to accretional and impact
512 vapor loss during planet formation (Wang et al., 2015; Wang and Jacobsen; 2016; Hin et al.,
513 2017). Such processes could have overprinted the primary stable isotopic composition since
514 magma crystallization, making it challenging to clarify the magmatic effects and conclude
515 unambiguous inferences. As one of the most refractory elements, Ca is resistant to evaporative
516 loss and therefore preserves mostly the initial magmatic signals. Boosted by the discovery of
517 notable isotopic fractionation during magmatic differentiation, Ca-isotopes are projected to serve
518 as a powerful technique in reconstructing the crustal evolution of differentiated planetary bodies
519 beyond the Earth-moon system, including Mars and Vesta, when coupled with other isotope
520 systems (Elkins-Tanton, 2012; Schiller et al., 2011; Schiller et al., 2017; Sedaghatpour and
521 Jacobsen, 2019).

522 6. Conclusions

523 We report high-precision Ca-isotope measurements for the late-Permian alkaline igneous suite in
524 the Øyangen Caldera, Oslo Rift, Norway. Major and trace element variations demonstrate a co-
525 genetic closed-system fractional crystallization sequence of the main-series samples, including
526 basanites, ring-dyke syenites, and central-dome syenites. We observe an indiscernible change in
527 $\delta^{44/40}\text{Ca}$ (< 0.05‰) from the basanite to the primitive ring-dyke syenites in the intermediate
528 magma and a remarkable increase in $\delta^{44/40}\text{Ca}$ (~0.53‰) among the evolved ring-dyke and

529 central-dome syenites in the felsic magma. The rise in $\delta^{44/40}\text{Ca}$ is most consistent with
530 equilibrium isotopic fractionation controlled by feldspar during fractional crystallization. Using a
531 regression approach, we constrain the $^{44}\text{Ca}/^{40}\text{Ca}$ fractionation factors for plagioclase and K-
532 feldspar facilitated by high precision Ca-isotope data. Integrated with a mineral fractionation
533 factor database, the new results reveal a general inverse correlation between Ca concentration
534 and extent of fractionation. K-feldspar carries the lightest $^{44}\text{Ca}/^{40}\text{Ca}$ among the major rock-
535 forming minerals of Earth's crust. Confirmation of substantial fractionation during magma
536 solidification promotes the utilization of Ca-isotopes in probing the history of igneous
537 differentiation in versatile scopes, from the evolution of a single magma chamber to
538 hypothesized global magma oceans.

539 **CRedit authorship contribution statement**

540 H.F., S.B.J., and B.T.L. conceptualized and initiated the project. H.F. performed analytical work,
541 developed the interpretation with input from S.B.J. and Z.T.E., and wrote the manuscript. All
542 authors reviewed and edited the manuscript to improve it. Z.T.E. provided Ca-isotope data for
543 rock standards. B.T.L. provided samples and geological context, elemental data for mineral
544 separates as well as preliminary data to show that this caldera was the perfect place for this
545 project. All authors discussed ideas and provided comments throughout the investigation.

546 **Declaration of competing interest**

547 The authors declare that they have no known competing financial interests or personal
548 relationships that could have appeared to influence the work reported in this paper.

549 **Acknowledgements**

550 We thank Yvan Gérard and Chris Parendo for helpful assistance in maintaining the Nu Sapphire
551 (SP001) mass spectrometer. We thank Mingzhen Yu for performing the MELTS calculations.
552 We thank Rajdeep Dasgupta for careful editorial handling. Finally, we are thankful to Scott
553 Angus MacLennan and an anonymous reviewer for constructive comments. This work was
554 partly supported by the DOE-NNSA grant #DE-NA0003904 and NASA Emerging Worlds
555 Program grant #80NSSC20K0346, both to S.B.J.

556 **References**

- 557 Allègre, C. J., Treuil, M., Minster, J.-F., Minster, B., Albarède, F., 1977. Systematic use of trace
558 element in igneous process. *Contributions to Mineralogy and Petrology* 60, 57–75.
- 559 Amsellem, E., Moynier, F., Bertrand, H., Bouyon, A., Mata, J., Tappe, S., Day, J. M. D., 2020.
560 Calcium isotopic evidence for the mantle sources of carbonatites. *Sci. Adv.* 6, eaba3269.
- 561 Antonelli M. A., Schiller M., Schauble E. A., Mittal T., DePaolo D. J., Chacko T., Grew E. S.,
562 Tripoli B., 2019a. Kinetic and equilibrium Ca isotope effects in high-T rocks and
563 minerals. *Earth Planet. Sci. Lett.* 517, 71–82.
- 564 Antonelli, M. A., Mittal, T., McCarthy, A., Tripoli, B. A., Watkins, J., DePaolo, D. J., 2019b. Ca
565 isotopes record rapid crystal growth in volcanic and subvolcanic systems. *Proc. Natl.*
566 *Acad. Sci.*, 116, 20315–20321.
- 567 Antonelli M. A., Simon J. I., 2020. Calcium isotopes in high-temperature terrestrial processes.
568 *Chem. Geol.* 548 119–651.
- 569 Brewer, A. W., Teng F-Z, Mullen, E., 2018. Magnesium Isotopes as a Tracer of Crustal
570 Materials in Volcanic Arc Magmas in the Northern Cascade Arc. *Front. Earth Sci.* 6:21.
- 571 Cashman, K., Giordano, G., 2014. Calderas and magma reservoirs. *Journal of Volcanology and*
572 *Geothermal Research*, 288, 28–45.
- 573 Chen, C., Dai, W., Wang, Z., Liu, Y., Li, M., Becker, H., Foley, S. F., 2019. Calcium isotope
574 fractionation during magmatic processes in the upper mantle. *Geochim. et Cosmochim.*
575 *Acta* 249, 121–137.
- 576 Corfu, F., Dahlgren, S., 2008. Perovskite U–Pb ages and the Pb isotopic composition of alkaline
577 volcanism initiating the Permo–Carboniferous Oslo Rift. *Earth Planet. Sci. Lett.* 256–269.
- 578 Corfu, F., Larsen, B. T., 2020. U–Pb systematics in volcanic and plutonic rocks of the
579 Krokskogen area: Resolving a 40 million years long evolution in the Oslo Rift. *Lithos*
580 376–377.
- 581 DePaolo, D. J., 1981. Trace element and isotopic effects of combined wallrock assimilation and
582 fractional crystallization. *Earth Planet. Sci. Lett.* 53, 189–202.
- 583 Elkins-Tanton, L. T., 2012. Magma oceans in the inner solar system. *Annu. Rev. Earth Planet.*
584 *Sci.* 40, 113–139.
- 585 Eriksen, Z. T., Jacobsen, S. B., 2022. Calcium isotope constraints on OIB and MORB
586 petrogenesis: The importance of melt mixing. *Earth Planet. Sci. Lett.* 593, 117665.
- 587 Feng, C., Qin, T., Huang, S., Wu, Z., Huang, F., 2014. First-principles investigations of
588 equilibrium calcium isotope fractionation between clinopyroxene and Ca-doped
589 orthopyroxene. *Geochim. Cosmochim. Acta* 143, 132–142.
- 590 Feng, L., Zhou, L., Yang, L., Zhang, W., Wang, Q., Shuoyun, T., Hu, Z., 2018. A rapid and
591 simple single-stage method for Ca separation from geological and biological samples for
592 isotopic analysis by MC-ICP-MS. *J. Anal. At. Spectrom.* 33, 413–421.
- 593 Gavrilenko, M., Ozerov, A. Y., Kyle, P. R., Carr, M. J., Nikulin, A., Vidito, C., Danyushevsky,
594 L., 2016. Abrupt transition from fractional crystallization to magma mixing at Gorely
595 volcano (Kamchatka) after caldera collapse. *Bulletin of Volcanology*, 78, 1–28.

- 596 Gualda G. A. R., Ghiorso M. S., Lemons R. V., Carley T. L., 2012. Rhyolite-MELTS: a
597 modified calibration of MELTS optimized for silica-rich, fluid-bearing magmatic systems.
598 *J. Petrol.* 53, 875–890.
- 599 Hin, R. C., Coath, C. D., Carter, P. J., Nimmo, F., Lai, Y., Pogge von Strandmann, P.A.,
600 Willbold, M., Leinhardt, Z.M., Walter, M.J., Elliott, T., 2017. Magnesium isotope
601 evidence that accretional vapour loss shapes planetary compositions. *Nature*, 549, 511–
602 515.
- 603 Huang F., Zhou C., Wang W., Kang J., Wu Z., 2019. First- principles calculations of equilibrium
604 Ca isotope fractionation: Implication for oldhamite formation and evolution of lunar
605 magma ocean. *Earth Planet. Sci. Lett.* 510, 153–160.
- 606 Huang, S., Farkaš, J., Jacobsen, S. B., 2010. Calcium isotopic fractionation between
607 clinopyroxene and orthopyroxene from mantle peridotites. *Earth Planet. Sci. Lett.* 292,
608 337–344.
- 609 Huang, S., Farkaš, J., Jacobsen, S. B., 2011. Stable calcium isotopic compositions of Hawaiian
610 shield lavas: Evidence for recycling of ancient marine carbonates into the mantle.
611 *Geochim. et Cosmochim. Acta* 75, 4987–4997.
- 612 Johnson, C. M., Beard, B. L., Albarède, F., 2004. Overview and General Concepts. *Rev Mineral.*
613 *and Geochem.* 55, 1–24.
- 614 Klaver, M., Luu, T. H., Lewis, J., Jansen, M. N., Anand, M., Schwieters, J. B., Elliott, T., 2021.
615 The Ca isotope composition of mare basalts as a probe into the heterogeneous lunar
616 mantle. *Earth Planet. Sci. Lett.* 570, 117079.
- 617 Kang, J.-T., Ionov, D. A., Liu, F., Zhang, C.-L., Golovin, A. V., Qin, L.-P., Zhang, Z.-F., Huang,
618 F., 2017. Calcium isotopic fractionation in mantle peridotites by melting and
619 metasomatism and Ca isotope composition of the Bulk Silicate Earth. *Earth Planet. Sci.*
620 *Lett.* 474, 128–137.
- 621 Larsen, B. T., Olaussen, S., Sundvoll, B., Heeremans, M., 2008. The Permo-Carboniferous Oslo
622 Rift through six stages and 65 million years. *Episodes* 31, 52–58.
- 623 Lamminen, J., Andersen, T., Nystuen, J. P., 2011. Zircon U-Pb ages and Lu-Hf isotopes from
624 basement rocks associated with Neoproterozoic sedimentary successions in the
625 Sparagmite Region and adjacent areas, South Norway: the crustal architecture of western
626 Baltica. *Norsk Geologisk Tidsskrift* 91, 35–55.
- 627 Li, Y., Wu, Z., Huang, S., Wang, W., 2022. Pressure and concentration effects on intermineral
628 calcium isotope fractionation involving garnet. *Chem. Geol.* 591, 120–722.
- 629 McDonough, W. F., Sun, S.-S., 1995. The composition of the Earth. *Chem. Geol.* 120, 223–253.
- 630 Neumann, E.-R., Larsen, B. T., Sundvoll, B., 1985. Compositional variations among gabbroic
631 intrusions in the Oslo rift. *Lithos*, 18, 35–59.
- 632 Neumann, E.-R., Olsen, K. H., Baldrige, W. S., Sundvoll, B., 1992. The Oslo Rift: A review.
633 *Tectonophysics* 208, 1–18.
- 634 Neumann, E.-R., Wilson, M., Heeremans, M., Spencer, E. A., Obst, K., Timmerman, M. J.,
635 Kirstein, L., 2004. Carboniferous-Permian rifting and magmatism in southern

- 636 Scandinavia, the North Sea and northern Germany: a review. *Geol. Soc. Specc Publ.* 223,
637 11–40.
- 638 O’Hara, M. J., 1977. Geochemical evolution during fractional crystallization of a periodically
639 refilled magma chamber. *Nature* 266, 503–507.
- 640 Russell, W., Papanastassiou, D. A., Tombrello, T. A., 1978. Ca isotope fractionation on the Earth
641 and other solar system materials. *Geochim. et Cosmochim. Acta*, 42, 1075–1090.
- 642 Sedaghatpour, F., Jacobsen, S. B., 2019. Magnesium stable isotopes support the lunar magma
643 ocean cumulate remelting model for mare basalts. *Proc. Natl. Acad. Sci.* 116, 73–78.
- 644 Schiller, M., Baker, J. A., Creech, J., Paton, C., Millet, M.-A., Irving, A., Bizzarro, M., 2011.
645 Rapid timescales for magma ocean crystallisation on the howardite–eucrite–diogenite
646 parent body. *Astrophys. J.* 740, L22.
- 647 Schiller, M., Dallas, J., Creech, J., Bizzarro, M., Baker, J., 2017. Tracking the formation of
648 magma oceans in the Solar System using stable magnesium isotopes. *Geochem. Perspect.*
649 *Lett.* 3, 22–31.
- 650 Sun, J., Zhu, X.-K., Belshaw, N. S., Chen, W., Doroshkevich, A. G., Luo, W.-J., Song, W.-L.,
651 Chen, B.-B., Cheng, Z.-G., Li, Z.-H., Wang, Y., Kynicky, J., Henderson, G. M., 2021. Ca
652 isotope systematics of carbonatites: Insights into carbonatite source and evolution.
653 *Geochem. Persp. Lett.* 17, 11–15.
- 654 Tera, F., Eugster, O., Burnett, D. S., Wasserburg, G. J., Comparative study of Li, Na, K, Rb, Cs,
655 Ca, Sr and Ba abundances in achondrites and in Apollo 11 lunar samples, 1970.
656 *Proceedings of the Apollo 11 Lunar Science Conference.* 2, 1673–1657.
- 657 Teng, F., Dauphas, N., Watkins, J., 2017. Non-Traditional Stable Isotopes: Retrospective and
658 Prospective. *Rev Mineral. and Geochem.* 82, 1–26.
- 659 Valdes, M. C., Debaille, V., Berger, J., Armytage, R.M.G., 2019. The effects of high-
660 temperature fractional crystallization on calcium isotopic composition. *Chem. Geol.* 509,
661 77–91.
- 662 Wang (王阳), Y., He, Y., Wu, H., Zhu, C., Huang, S., Huang, J., 2019. Calcium isotope
663 fractionation during crustal melting and magma differentiation: Granitoid and mineral-
664 pair perspectives. *Geochim. et Cosmochim. Acta* 259, 37–52.
- 665 Watson, E. B., Müller, T., 2009. Non-equilibrium isotopic and elemental fractionation during
666 diffusion-controlled crystal growth under static and dynamic conditions. *Chem. Geol.* 267,
667 111–124.
- 668 Wang, K., Jacobsen, S. B., Sedaghatpour, F., Chen, H., Korotev, R. L., 2015. The earliest Lunar
669 Magma Ocean differentiation recorded in Fe isotopes. *Earth Planet. Sci. Lett.* 430, 202–
670 208.
- 671 Wang, K., Jacobsen, S.B., 2016. Potassium isotopic evidence for a high-energy giant impact
672 origin of the Moon. *Nature* 538, 487–490.
- 673 Wang, W.-Z., Qin, T., Zhou, C., Huang, S., Wu, Z., Huang, F., 2017a. Concentration effect on
674 equilibrium fractionation of Mg–Ca isotopes in carbonate minerals: insights from first-
675 principles calculations. *Geochim. Cosmochim. Acta* 208, 185–197.

- 676 Williamson, J., 1968. Least-squares fitting of a straight line. *Can. J. Phys.* 46, 1845–1847.
- 677 Wright, T. L., Doherty, P. C., 1970. A Linear Programming and Least Squares Computer
678 Method for Solving Petrologic Mixing Problems. *Geol. Soc. Am. Bull.* 81, 1995–2008.
- 679 Yoshimura, Y., Motoyoshi, Y., Miyamoto, T., 2008. Sapphirine+quartz association in garnet:
680 implication for ultrahigh-temperature metamorphism at Rundvågshetta, Lützow-Holm
681 Complex, East Antarctica. *Geol. Soc. Spec. Publ.* 308, 377–390.
- 682 Young E. D., Galy A., Nagahara H., 2002. Kinetic and equilibrium mass-dependent isotope
683 fractionation laws in nature and their geochemical and cosmochemical significance.
684 *Geochim. Cosmochim. Acta* 66, 1095–1104.
- 685 Zhang, H., Wang, Y., He, Y., Teng, F.-Z., Jacobsen, S. B., Helz, R. T., Marsh, B. D., Huang, S.,
686 2018. No Measurable Calcium Isotopic Fractionation During Crystallization of Kilauea
687 Iki Lava Lake. *Geochem., Geophys., Geosys.* 19, 3128–31
- 688 Zhu, H., Liao, R., Liu, H., Du, L., Li, H., Li, C., Zhang, Z., Sun, W., 2021. Calcium isotopic
689 fractionation during magma differentiation: Constraints from volcanic glasses from the
690 eastern Manus Basin. *Geochim. Cosmochim. Acta* 305, 228–242.